Differential tissue deformability underlies shape divergence of the embryonic brain and spinal cord under fluid pressure

Susannah B.P. McLaren[1,2,*], Shi-Lei Xue[3], Siyuan Ding[1,2], Alex Winkel[2], Oscar Baldwin[1,2], Shreya Dwarakacherla[1,2], Kristian Franze[2,4], Edouard Hannezo[3], Fengzhu Xiong[1,2,*]

[1] Wellcome Trust / CRUK Gurdon Institute, University of Cambridge, Cambridge, UK

[2] Department of Physiology, Development and Neuroscience, University of Cambridge, Cambridge, UK

[3] Institute of Science and Technology Austria, Klosterneuburg, Austria

[4] Friedrich-Alexander-Universität Erlangen-Nürnberg, Germany; Max-Planck-Zentrum für Physik und Medizin, Germany

[*]Correspondence: sbm35@cam.ac.uk; fx220@cam.ac.uk

ABSTRACT

An expanded brain enables the complex behaviours of vertebrates that promote their adaptation in diverse ecological niches[1–3]. Initial morphological differences between the brain and spinal cord emerge as the antero-posteriorly patterned neural plate folds to form the neural tube[4–7] during embryonic development. Following neural tube closure, a dramatic expansion of the brain diverges its shape from the spinal cord[8], setting their distinct morphologies for further development[9,10]. How the brain and the spinal cord expand differentially remains unclear. Here, using the chicken embryo as a model, we show that the hindbrain expands through dorsal tissue thinning under a positive hydrostatic pressure from the neural tube lumen[11,12] while the dorsal spinal cord shape resists the same pressure. Using magnetic droplets and atomic force microscopy, we reveal

that the dorsal tissue in the hindbrain is more fluid than in the spinal cord. The dorsal hindbrain harbours more migratory neural crest cells[13] and exhibits reduced apical actin and a disorganised laminin matrix compared to the dorsal spinal cord. Blocking the activity of neural crest-associated matrix metalloproteinases inhibited dorsal tissue thinning, leading to abnormal brain morphology. Transplanting early dorsal hindbrain cells to the spinal cord was sufficient to create a region with expanded brain-like morphology including a thinned-out roof. Our findings open new questions in vertebrate head evolution and neural tube defects, and suggest a general role of mechanical pre-pattern in creating shape differences in epithelial tubes.

MAIN

The neural tube gives rise to the brain and spinal cord during vertebrate embryonic development. In avian embryos, the volumetric expansion of the brain over a relatively stable spinal cord takes place shortly after neural tube closure (Figure 1A) and depends on the hydrostatic pressure from the neural tube lumen[14,11]. In the stages prior to brain expansion (before Hamburg-Hamilton (HH) stage 13[8]), the neural tube has large openings at both the anterior and posterior ends that allow fluid to move between the tube lumen and its surroundings (Figure 1B). These openings narrow and close concomitant with the onset of brain expansion around HH13[15], such that the neural tube lumen becomes a closed and continuous fluid filled cavity (Figure S1A). Consistent with pioneering studies[16], we recorded a positive internal lumen pressure of ~15Pa in the initial stages of brain expansion (HH13-15), which increased to ~25Pa as brain expansion progressed (HH19-21. Figure 1C and S1B). To assess how neural tube morphology changes as internal lumen pressure increases, we measured tissue thickness around the circumference of the lumen in cross sections of the

hindbrain and spinal cord prior to and after brain expansion (HH11 and HH16, respectively. Figure 1D-F). Dorsal hindbrain tissue approximately halved in thickness and formed a single-cell thick epithelium concomitant with brain expansion, whilst little dorsal thinning or tissue shape change was observed in the spinal cord (Figure S1C and D).

To test the role of lumen pressure in dorsal thinning, we intubated[14] embryos in the brain or spinal cord just prior to brain expansion (HH11), leaving the tube lumen connected to the embryo's surroundings to equate the pressure (Figure S1E). Although we observed an increase in hindbrain cross-sectional area, in line with proliferation and tissue growth, dorsal hindbrain thinning and expansion were inhibited in intubated embryos following 20 hours of incubation (Figure 1G, I and J). Not only brain-intubated but also a spinal cord-intubated embryo showed inhibited hindbrain thinning, confirming that the lumen is connected along the anterior-posterior axis of the neural tube and the tissues experience the same hydrostatic pressure. Conversely, treating embryos with β-D-xyloside (BDX) [17], which has been found to osmotically increase lumen pressure by ~30% [12], led to an increase in expansion and extension of the thinned dorsal roof in the hindbrain and a moderately enlarged spinal lumen with no dorsal thinning (Figure 1H, K and L). Together these findings demonstrate that neural tube lumen pressure drives dorsal tissue thinning in the hindbrain but is resisted in the dorsal spinal cord, leading to brain expansion relative to the spinal cord.

The differential thinning of dorsal tissue between the hindbrain and the spinal cord may result from a few scenarios. First, different initial tissue curvature at the onset of pressure increase (Figure 1D) can lead to diverging dynamics of thinning and volume expansion. To explore this possibility, we formulated a physical model describing the neural tube as a

cellularised, homogeneous material under internal pressure (Supplemental Text 1). The model predicted that regions of the tube with a greater initial radius (lower curvature) will expand more in the short-term than parts of the tube with an initially smaller radius (higher curvature) as circumferential stress will be higher in low curvature regions (Figure 2A and A'), which is consistent with the shape dynamics observed in the hindbrain and the spinal cord. To experimentally test this possibility, we modified spinal cord lumen shape prior to brain expansion by performing *in ovo* surgeries to remove somites and anterior presomitic mesoderm on either side of the spinal cord (Figure 2B). This operation releases tissue confinement from not only the somites (Figure S2A) but also the dorsal non-neural ectoderm as it was cut through during somite ablation. After ~20 hours of incubation, these embryos healed and exhibited reduced spinal cord dorsal curvature and in one case clear rounding of the spinal cord cross section (Figure 2C, S2B-C). However, this did not lead to the formation of a thinned-out roof, as was observed in the hindbrain (Figure S2D). These results suggest that the higher curvature of the spinal cord dorsal region is not sufficient to explain the lack of dorsal tissue thinning in the spinal cord. At the same time, this experiment ruled out a second alternative model in which local confinement from neighbouring tissues (such as somites and the presomitic mesoderm) might modulate neural tube shape ([18] and Figure S2A) by constraining lumen expansion of the spinal cord relative to the hindbrain. This led us to explore a third hypothesis: that the differential expansion of the brain and spinal cord was due to the dorsal tissue of the hindbrain being more deformable than that of the spinal cord, enabling local thinning despite a spatially uniform hydrostatic pressure. To test whether the material properties of the hindbrain and spinal cord dorsal tissue differed before the onset of increased lumen pressure, we injected ferrofluid oil droplets into the forebrain of HH11 embryos and positioned the droplets in either the hindbrain or spinal cord using a magnetic

field (Figure 2D). We then observed the resulting tissue deformation from the stress generated by the droplets as they minimize surface tension after removal of the magnetic field (Figures 2E). Droplets were injected either at equal volumes (2nl) or at a ratio to account for the difference in initial lumen size (4nl in the larger hindbrain lumen, 1nl in the smaller spinal cord lumen). In both cases the droplets showed a higher curvature at the droplet-lumen interface in the spinal cord, indicating a higher pressure was exerted on the spinal cord tissue than the hindbrain by this mechanical perturbation (Figure S2E). Still, the thickness change of dorsal tissue at the droplet site was greater in the hindbrain than in the spinal cord (Figure 2F), indicating that hindbrain dorsal tissue was more deformable. To directly measure tissue mechanical properties, we used an atomic force microscopy (AFM) cantilever to indent the dorsal region of the hindbrain and spinal cord (Figure 2G) in the same embryos and measure tissue relaxation in response to a sustained force (50 or 75nN). We found that the dorsal hindbrain had a higher fluidity than that of the spinal cord prior to brain expansion, whilst no significant difference in instantaneous elastic modulus was detected (Figure 2H and I). While *in vivo* AFM measurements may contain a contribution of differences from other non-local structures such as the extracellular matrix (ECM) anchoring the neural tube, these results further support the hypothesis that the dorsal hindbrain will deform more than the dorsal spinal cord under the same lumen pressure.

To investigate the mechanism of dorsal tissue deformability, we explored the cellular organisation of the tissue at stages leading up to brain expansion (HH9-12). The dorsal neural tube tissue is occupied by neural crest cells that reorganise their actomyosin cytoskeleton as they undergo an epithelial-to-mesenchymal transition (EMT) and delaminate from the tube dorsal surface as the walls of the neural plate fuse dorsally [19,20,21]. The

121 dynamics of neural crest delamination between cranial and trunk regions is known to differ
122 [22,23], making them an exciting candidate for underlying tissue intrinsic differences between
123 the dorsal hindbrain and spinal cord. We observed clear apical organisation of actin and
124 myosin within the dorsal spinal cord in HH12 embryos, however this organisation was largely
125 absent in the neural crest domain of the hindbrain (Figure 3A-C). This change in cytoskeleton
126 organisation indicated that a transition away from an epithelial cell state to a more
127 mesenchymal cell state was occurring in the dorsal hindbrain. A key player in this process is
128 the zinc-finger transcription factor Snail2 which is expressed in the pre-migratory and early
129 migrating neural crest [24,25]. Using Snail2 as a marker, we observed that the dynamics of
130 neural crest delamination and migration at the dorsal surface of the neural tube differed
131 between the hindbrain and the spinal cord leading up to brain expansion (HH9-12), with
132 Snail2+ cells migrating in a cell-by-cell fashion in spinal cord regions, whilst those in the
133 hindbrain migrate in a collective wave (Figure 3D and S3A). Neural crest cells utilise matrix
134 metalloproteases (MMPs) to remodel the surrounding ECM [26,27]. ECM architecture plays an
135 important role in determining tissue material properties, with higher levels of ECM
136 organisation conferring greater stiffness (or elasticity) and more disordered matrix
137 organisation leading to softening (or a more viscous behaviour) [28,29], which contributes to
138 long-term deformability.
139
140 This led us to investigate ECM organisation in the hindbrain and the spinal cord as a potential
141 mediator of tissue deformability. Cross-sectional views showed that laminin was
142 redistributed throughout the dorsal hindbrain in the premigratory neural crest domain,
143 whilst comparatively little redistribution was observed in the dorsal spinal cord (Figure 3E).
144 This was associated with a more sparce laminin coating of the hindbrain compared to the

145 spinal cord when viewed from the dorsal side (Figure 3F and S3B and C). These findings
146 suggest that ECM is being actively reorganised and redistributed out of the plane of the
147 basement membrane to a greater extent in the hindbrain.
148
149 To test whether ECM remodelling plays a role in dorsal hindbrain thinning, we inhibited
150 MMP activity in embryos prior to brain expansion stages using an MMP-specific small
151 molecule inhibitor (GM6001, 1000µM). Brain expansion was reduced in inhibitor treated
152 embryos and a smaller surface area of the dorsal hindbrain was apparent (Figure 3G-H). In
153 embryos with obvious observable developmental defects (0/6 control, 4/8 inhibitor treated),
154 the hindbrains did not undergo dorsal thinning and in some cases aggregated a mass of
155 Snail2+ cells within the lumen (Figure S3D). In embryos that developed normally overall (6/6
156 control, 4/8 inhibitor treated), the hindbrains of the treated embryos showed thicker or
157 shorter dorsal roofs than those of the controls (Figure 3I, J and S3D). The laminin surface
158 covering the basal extent of the dorsal hindbrain appeared less disrupted in embryos with
159 inhibited roof thinning (Figure 3I) and the dorsal tissue was still populated with Snail2+ cells,
160 suggesting that neural crest specification continued in the presence of the inhibitor.
161 Together, these data are consistent with the idea that neural crest mesenchymal behaviour
162 and subsequent ECM remodelling is required for thinning and expansion of the dorsal
163 hindbrain.
164 To definitively test the intrinsic ability of early hindbrain dorsal cells to generate a thinned
165 roof under lumen pressure, we performed an *in ovo* graft experiment, moving a small piece
166 of dorsal hindbrain (or spinal cord as a control) tissue from a GFP+ embryo to the pre-cut
167 dorsal region of the spinal cord of a wildtype host before the onset of lumen pressure
168 (Figure 4A). Re-integration of the graft to reform a closed neural tube that would continue

169 normal morphogenesis was expected to be rare given the difficulty of positioning the graft in
170 such a small incision site and maintaining contact between the small graft and the host
171 tissue. After overnight culture, we found 5 embryos with different degrees of hindbrain
172 dorsal tissue integration into the spinal cord, and 2 spinal cord-to-spinal cord controls (Figure
173 4B, S4A and S4B). The control embryos exhibited a thick dorsal region at the grafted site
174 (Figure 4C, D and S4B, 2/2 embryos). Interestingly, 2 hindbrain-to-spinal cord grafted
175 embryos exhibited dorsal tissue thinning in the grafted region (Figure 4C, D and S4B). In the
176 cleanest graft where the donor tissue completely replaced the host dorsal region, we found
177 a distinctively thinned out dorsal roof and hindbrain-like morphology specific to the grafted
178 region (Figure 4C), with a thicker spinal cord-like host dorsal region present on the anterior
179 and posterior sides of the graft. Cells in the grafted region were Snail2+ (Figure 4E) and the
180 thinned-out roof coincided with loss of apical actin localisation (Figure S4C), suggesting that
181 the grafted region contained premigratory neural crest cells undergoing EMT. This striking
182 ability of Snail2+ dorsal hindbrain cells to form a thinned-out and elongated roof in the
183 spinal cord region suggests that hindbrain premigratory neural crest cells are sufficient to
184 drive dorsal tissue thinning in response to lumen pressure.
185
186 Taken together, our findings support a mechanism where deformability of the neural tube
187 dorsal tissue and ECM organisation underlie the distinct shape changes of the brain and the
188 spinal cord under a shared lumen pressure (Figure 4F). These differences likely result from
189 different behaviours of the neural crest cells, which are known to exhibit different signalling,
190 metabolism and fates between cranial and trunk levels. Our study thus implies a closely
191 coordinated initial developmental step coupling brain expansion and neural crest EMT, both
192 essential contributors to the formation and evolution of the vertebrate head [30]. We note

that these findings are in agreement with classic chimera grafting experiments in which reduced dorsal roof thinning and elongation can be observed in hindbrain regions lacking neural crest cells [31]. Irregularly shaped mesenchymal cells in the dorsal hindbrain have also been observed to contribute to the formation of a thinned out hindbrain roof as the narrow lumen of the zebrafish brain undergoes expansion [32], suggesting that neural crest mediated dorsal tissue fluidisation may contribute to brain expansion in other species. Future work will resolve the detailed molecular and cellular regulation of dorsal neural tissue mechanics and identify genetic and environmental factors that may cause developmental defects associated with aberrant brain expansion through this mechanism. Given the role of lumen pressure in driving morphogenesis of a variety of epithelial tissues and organs [33,34,35,36] our findings here in the neural tube imply a general strategy for creating diverse biological shapes via a mechanical property pre-pattern before the onset of changes in fluid pressure.

ACKNOWLEDGEMENTS

We thank A. Dimitracopoulos, K. Kawaguchi, J. Vidigueira, B. Baum, I. McLaren and members of the Buckley, Scarpa, Steventon, Kawaguchi and Xiong labs for technical assistance and constructive feedback. We thank Ryan Greenhalgh for methods developed to obtain fluidity values from AFM data. We thank Nicola Lawrence, Alex Sossick and Sargon Gross-Thebing from the Gurdon Institute Imaging Facility for microscopy support. This work was supported by a Wellcome Trust / Royal Society Sir Henry Dale Fellowship (215439/Z/19/Z) and an UKRI-EPSRC Frontier Research Grant (EP/X023761/1, originally selected as an ERC Starting Grant) to F.X.

AUTHOR CONTRIBUTION

S.B.P.M and F.X. conceived the project, designed experiments and wrote the manuscript. S.B.P.M performed all experiments and analysed the data. S.X and E.H. developed the theoretical model. S.D, O.B, S.D and F.X contributed to embryo experiments. K.F. and A.W. designed and performed AFM experiments.

MATERIALS & METHODS

Egg lines and embryo culture. Wild type fertilised chicken eggs were obtained from MedEgg Inc., GFP+ eggs (Cytoplasmic [37]and Membrane[38]) were obtained from the National Avian Research Facility (NARF) at University of Edinburgh. Eggs were kept in a fridge at 14°C for storage and in a 37.5°C humidified (40%-60%) incubator (Brinsea) during incubation. No animal protocol under the UK Animals (Scientific Procedures) Act 1986 was required for the chicken embryo stages investigated (incubated under 2 weeks, or 2/3 of the gestation time). *Ex ovo* culture was performed using a modified EC culture[39] protocol as described[40]. For *in ovo* operations, egg shells were windowed with surgical scissors after removing some albumen. A small volume of Chinese calligraphy ink (YiDeGe, Black) was then injected underneath the embryo to help with visualisation. After performing surgical, mechanical or chemical perturbations, eggs were resealed with clear plastic tape and returned to incubation.

Pressure measurement. Pressure measurements were performed as detailed in [41]. Briefly, a glass microneedle connected to a pressure sensor was inserted into the neural tube lumen of chicken embryos at varying stages of development. Pressure readings were continuously recorded to include the pressure just outside the lumen, after insertion into the lumen, and after retraction from the lumen for each experiment. The pressure difference between the outside and inside of the lumen was taken as the neural tube lumen pressure.

241 Measurements where no stable pressure reading could be obtained inside the neural tube
242 lumen, likely due to needle clogging by tissue debris during the insertion, were excluded
243 from analysis.
244 Pressure modulation. Intubation experiments were performed by inserting an open-ended
245 short glass capillary tube into the forebrain or spinal cord region of HH10-12 stage embryos.
246 Control experiments were performed by either inserting a glass capillary into tissues just
247 neighbouring the neural tube or inserting a very narrow glass capillary and not submerging it
248 in fluid with the embryo. β-D-xyloside (BDX) experiments were performed by adding either
249 DMSO or BDX to embryo culture medium at a final concentration of 2mM in L15 media. In all
250 cases embryos were cultured overnight *ex ovo*. Only embryos that displayed continued
251 development were included in the analysis.
252 Assessment of lumen continuity. Fluorescently labelled Dextran was injected into the neural
253 tube lumen of HH11-13 stage embryos. The fluorescent signal was imaged following
254 injection to assess how far the dye travelled along the neural tube lumen. The dye was
255 observed to spread anteriorly into the brain region and posteriorly into the posterior spinal
256 cord when injected into the spinal cord lumen mid-way along the trunk.
257 Removal of confining tissues. Posterior somites and anterior presomitic mesoderm were
258 removed from embryos *in ovo* using a sharpened tungsten needle. The vitelline membrane
259 was peeled back and cuts were made at the interface between the spinal cord region of the
260 neural tube and posterior somites and anterior presomitic mesoderm. Somites and
261 presomitic mesoderm were peeled away to leave the posterior spinal cord unconfined on its
262 sides. Eggs were then resealed and incubated overnight. Embryos that showed a good
263 degree of healing and no obvious spinal cord ruptures were included in analysis.

264 Grafting experiments. Small patches of dorsal hindbrain or spinal cord cells from GFP
265 positive HH10-11 embryos were transplanted into the posterior spinal cord of stage-
266 matched wild type embryos. A sharpened tungsten needle was used to peel back the
267 vitelline membrane of donor and host embryos and to dissect out a small patch of dorsal
268 cells from either the hindbrain or spinal cord. Tissue patches were transferred using a Gilson
269 pipette and Ringers solution to the host embryos. A small incision was made into the
270 posterior host embryo dorsal neural tube and tissue patches were pushed into this incision.
271 Embryos were cultured *in ovo* overnight.
272 Ferrofluid droplet experiments. Ferrofluid oil droplets were injected into the forebrain region
273 of HH10-12 stage embryos using a Nanojet injector set to inject a volume of either 1, 2, or
274 4nl. Droplets were positioned in the lumen of either the hindbrain or spinal cord using a
275 magnet and custom-built embryo holder. Embryos were fixed approximately 1.5 hours post
276 droplet injection prior to immunostaining and confocal imaging or imaged live. Dorsal roof
277 tissue thickness was measured at the point of maximum roof deformation in the hindbrain
278 and spinal cord of injected embryos at the droplet location. Uninjected embryos at
279 equivalent stages were measured at the same anterior-posterior level as controls.
280 Atomic force microscopy. Atomic force microscopy (AFM) indentation measurements were
281 performed using the setup described in [42]. Briefly, HH10-12 stage chicken embryos were
282 cultured on agarose plates and the vitelline membrane was removed to expose the embryo's
283 dorsal hindbrain and spinal cord. 89.3 µm diameter polystyrene beads were glued to Arrow-
284 TL1 cantilevers (nominal spring constant = 0.01 N/m; NanoWorld, Neuchâtel, Switzerland) as
285 probes. During measurements, the cantilever was approached with 10 µm/s until an
286 indentation force of either 50nN or 75nN was reached. This force was maintained for 3
287 seconds, thus enabling the acquisition of the deformation over time ('creep').

In order to extract fluidity and elastic modulus values from the force-distance curves, [43] introduced the following piecewise model for the force ramp:

$$F(t) = F_C \begin{cases} 0\,; & t < t_C \\ \left(\dfrac{t - t_C}{\Delta t_A}\right)^{\alpha}\,; & t_C \le t < t_C + \Delta t_A \\ 1\,; & t \ge t_C + \Delta t_A \end{cases}$$

where F_C is the magnitude of the applied force during the creep measurement reached in time Δt_A and applied for time t_C. α describes the shape of the force ramp ($1 < \alpha < 2$), where α = 1 corresponds to a linear force ramp and α closer to 2 to a polynomial force ramp. Fitting this equation yields F_C, t_C, Δt_A, and α . These values then derive the following equation for the indentation δ, here modified by substituting $E_0/(1-\nu^2)$ with the reduced instantaneous elastic stiffness, k_0

$$\delta(t) = \left[\frac{3}{4}\frac{1}{k_0\sqrt{R}} F_C \frac{\alpha(t - t_C)^{\alpha+\beta}}{\Delta t_A^{\alpha} t_0^{\beta}} B\left(\frac{\Delta t_A}{t - t_C}; \alpha, \beta + 1\right)\right]^{2/3}$$

where R is the radius of the bead, $B()$ is the incomplete beta function and the exponent, and β is the fluidity, which can have values ranging from 0 (for an elastic solid) to 1 (for a viscous fluid). Mean values for k_0 and β were determined from measurements taken across the hindbrain and along the spinal cord. Values obtained for k_0 were close to values obtained for the reduced apparent elastic modulus $K = E_0/(1-\nu^2)$ obtained by fitting the Hertz model $F = {}^{4}/_{3}\, K\delta^{3/2}\sqrt{R}$ to the instantaneous indentation data (Figure. S2).

<u>MMP inhibitor treatment.</u> After removal of the vitelline membrane covering the brain, 20µl of 1000µM broad-spectrum MMP inhibitor (GM6001) or DMSO diluted in Ringers solution, was added to the dorsal surface of HH10-11 stage embryos *in ovo.* Embryos were incubated overnight.

308 Immunostaining. After fixing embryos overnight in 500µl 4% PFA at 4°C, they were washed
309 3X for ~20 minutes per wash in 0.5% Triton-X- 100 (Sigma-Aldrich, X100) in PBS (PBST).
310 Embryos were incubated in blocking solution consisting of 4% Donkey serum in PBST for 1
311 hour at room temperature. Primary antibodies were diluted in blocking solution and
312 incubated with embryos for 2 days at 4°C. After washing embryos in PBST ~4 times over the
313 course of 2 hours, secondary antibodies, Hoecst and Phalloidin were diluted in blocking
314 solution and incubated with embryos for another 2 days at 4°C. Finally, embryos were
315 washed in PBST prior to imaging.
316 Primary and secondary antibodies used. Laminin (DSHB, 3H11) 1:100, Snail2 (Cell Signaling
317 Technology, 9585S) 1:200, pMLC2 (Cell Signaling Technology, 3671S) 1:100, Hoecst 1:1000,
318 Phalloidin 647 (Thermo Scientific, A22287) 1:500, Donkey Anti-Mouse 488n IgG (Abcam,
319 ab150105), Donkey Anti-Rabbit 594 (Abcam, ab150076)
320 Confocal imaging. Embryo cross sections and wholemounts were mounted on glass-bottom
321 confocal imaging dishes in VECTASHIELD (Vector Labs, H-1000-10) mounting medium. Z-
322 stacks were acquired at either 0.3 or 0.5µm z-steps using either an SP8 (Leica) or a SoRa
323 Spinning Disk (Nikon) using either a 10X, 20X or 40X objective.
324 Data analysis. All data analysis was performed in Python (www.python.org), with data stored
325 in Excel. Boxplots were obtained using the seaborn library and scatterplots using matplotlib.
326 Statistical analysis was performed using the scipy.stats Python library. Paired t-tests were
327 used to calculate p-values for the AFM data. Independent t-tests were used to calculate all
328 other p-values. Details of measurements of reported features are listed below:
329 1. Tissue shape analysis. The thickness profile of neural tube cross-sections was acquired by
330 measuring the radial tissue thickness along the lumen circumference starting from the
331 approximate mid-point of the dorsal hindbrain roof. For wildtype characterisation, the

332 distance along the lumen circumference was normalised for all samples so that tissue
333 thickness at distance '0' fell at the dorsal mid-point and tissue thickness at distance '1' at the
334 ventral midpoint of the neural tube cross section. A 4th degree polynomial was fit to the
335 thickness profiles to get an 'average' thickness profile for the hindbrain and spinal cord at
336 HH11 and HH16. Images acquired by confocal microscopy were visualised using either
337 ImageJ[44] or napari[45]. Cross sections were either visualised directly, or by reordering the axes
338 of image data acquired from wholemount samples in napari. For intubation experiment
339 analysis the mean thickness of the first 100µm of dorsal roof tissue from the dorsal midpoint
340 was compared. For BDX experiment analysis the mean thickness of the first 300µm of dorsal
341 roof tissue from the dorsal midpoint was compared. Equivalent positions along the hindbrain
342 were compared for assessing hindbrain roof thickness in MMP treated and control embryos.
343 2. Actin intensity along the apical surface. Curves were drawn along the apical surface of
344 neural tube cross sections starting from the dorsal midpoint and moving ventrally. The actin
345 intensity along the curve was measured using the ImageJ PlotProfile function. Normalised
346 average actin intensities along the apical surface were obtained for each embryo and binned
347 into three groups starting from the dorsal-most position and moving more ventrally. The
348 mean actin intensity for each embryo within each bin was plotted.
349 3. Somite removal analysis. Z planes were selected in the region where somite removal had
350 been performed and in a corresponding location in controls. Roof thickness was measured at
351 the dorsal midpoint for z planes from each embryo.

SUPPLEMENTAL TEXT 1

In this Supplementary note, we provide detailed analysis on morphological evolution of neural tube driven by luminal pressure. The brain and the spinal cord expand differentially under lumen pressure.

1. Elastic deformation of neural tube

The anterior and posterior ends of the neural tube get closed around Hamburg-Hamilton (HH) stage 13. After that, fluids accumulate in the enclosed lumen and tend to inflate the neural tube. To check if differences in the initial geometry and mechanical properties (such as elastic modulus) can explain the remarkable morphological differences between the hindbrain and spinal cord, especially the distinct radial expansion, after the neural tube pressurized with luminal fluids, here we extend previous model on the deformation of elastic tube after inflation[46] by including initial geometrical and mechanical inhomogeneities. The neural tube is modelled as an elastic, three-dimensional cylindrical membrane enclosed with a lumen filled with fluids. For simplicity, we consider initial shape of the neural tube is axisymmetric about A-P axis (defined as the Z-axis in Figure S5), but can be inhomogeneous along A-P axis: the initial radius $R = R(Z)$. The initial tissue thickness of the neural tube is assumed to be a constant H_0. Besides the axial and radial coordinates (R, Z) for the initial undeformed configuration, we also introduce the coordinates (r, z) for the current deformed configuration, as shown in Figure S5

Notice in both the undeformed and deformed configurations of the neural tube, the tissue surface is not necessarily parallel to the A-P axis (i.e. Z- or z-axis), but can derivate from it (see Figure S5 for schematic, where ϕ is the angle between the deformed tissue and z-axis). In this scenario, to evaluate the tissue stretching in the meridional direction, we introduce S and s to respectively track positions along the undeformed and deformed meridians.

First, we discuss the geometry of the deformed neural tube. The geometric variables in the deformed configuration satisfy

$$\frac{\mathrm{d}r}{\mathrm{d}s} = \sin\phi, \quad \frac{\mathrm{d}z}{\mathrm{d}s} = \cos\phi, \tag{1}$$

and the two principal curvatures of the deformed tissue are given by

$$\kappa_1 = -\frac{\mathrm{d}\phi}{\mathrm{d}s}, \quad \kappa_2 = \frac{\cos\phi}{r}, \tag{2}$$

where the subscript “1” and “2” respectively represent the meridional and azimuthal directions.

Second, we consider the mechanics of the neural tube. Pressurized with a luminal pressure, the tissue of the neural tube undergoes axial stretching λ_1 and radial expansion, which can be respectively quantified by the stretch ratios in the meridional and azimuthal directions:

$$\lambda_1 = \frac{\mathrm{d}s}{\mathrm{d}S}, \quad \lambda_2 = \frac{r}{R}. \tag{3}$$

The stretch ratio λ_α larger (or smaller) than 1 corresponds to tissue stretching (or compression) in that direction. Besides, such information on tissue deformation allows us to obtain the current thickness of the tissue H, which satisfies $H = H_0/(\lambda_1\lambda_2)$. To balance the luminal pressure P, the tissue forces T_1 and T_2 yield

$$T_1 = \frac{1}{2}\frac{Pr}{\cos\phi}, \tag{4}$$

$$T_1\kappa_1 + T_2\kappa_2 = P. \tag{5}$$

The relation between the tissue forces (T_1 and T_2) and tissue deformation (λ_1 and λ_2) is an intrinsic property of a tissue (or material). Such relation can be conveniently deduced by considering the stored elastic energy density of the tissue W. For incompressible materials such as soft tissue, $W = \mu f(\lambda_1, \lambda_2)$, with μ the initial shear modulus (a parameter used to quantify tissue stiffness). To include mechanical inhomogeneity in the hindbrain and spinal

cord, here we consider $\mu = \mu(Z)$. The tissue forces are related to tissue deformation as $T_1 = \frac{H_0}{\lambda_2}\frac{\partial W}{\partial \lambda_1}$, $T_2 = \frac{H_0}{\lambda_1}\frac{\partial W}{\partial \lambda_2}$. Hereafter, we use $w_\alpha = \partial W/\partial \lambda_\alpha$ for notational convenience.

The above equation system (1)-(5) can be recast as

$$\begin{aligned}
\frac{\mathrm{d}\lambda_1}{\mathrm{d}Z} &= \frac{1}{Rw_{11}}[\sin\phi\,(w_2 - w_{12}\lambda_1)S' + (w_{12}\lambda_2 - w_1)R'] - \frac{1}{w_{11}}\frac{\partial w_1}{\partial \mu}\mu', \\
\frac{\mathrm{d}\lambda_2}{\mathrm{d}Z} &= \frac{1}{R}(\sin\phi\,\lambda_1 S' - \lambda_2 R'), \\
\frac{\mathrm{d}\phi}{\mathrm{d}Z} &= \frac{\cos\phi}{R}\left(\frac{w_2}{w_1} - 2\frac{\lambda_1}{\lambda_2}\right)S', \\
\frac{\mathrm{d}z}{\mathrm{d}Z} &= \lambda_1\cos\phi\,S'.
\end{aligned} \tag{6}$$

where $R' = \mathrm{d}R/\mathrm{d}Z$, $S' = \mathrm{d}S/\mathrm{d}Z$, and $\mu' = \mathrm{d}\mu/\mathrm{d}Z$.

In the end, the elastic deformation of the pressurized neural tube is controlled by the differential equation system (6) with four unknows: two stretch ratios λ_1 and λ_2, the angle ϕ, and the axial position z.

In the development and morphogenesis of the neural tube, the brain region gradually bulges up and the spinal cord stays in a slim shape. We choose the middle point of the brain as the starting point of our calculation, and set $z(0) = 0$. Due to the symmetry of the bulge, we have $\phi(0) = 0$. The posterior end of the spinal cord can be approximated as $\lambda_2(L) = 1$, which would not affect the theoretical profile of the neural tube.

412 **Figures**

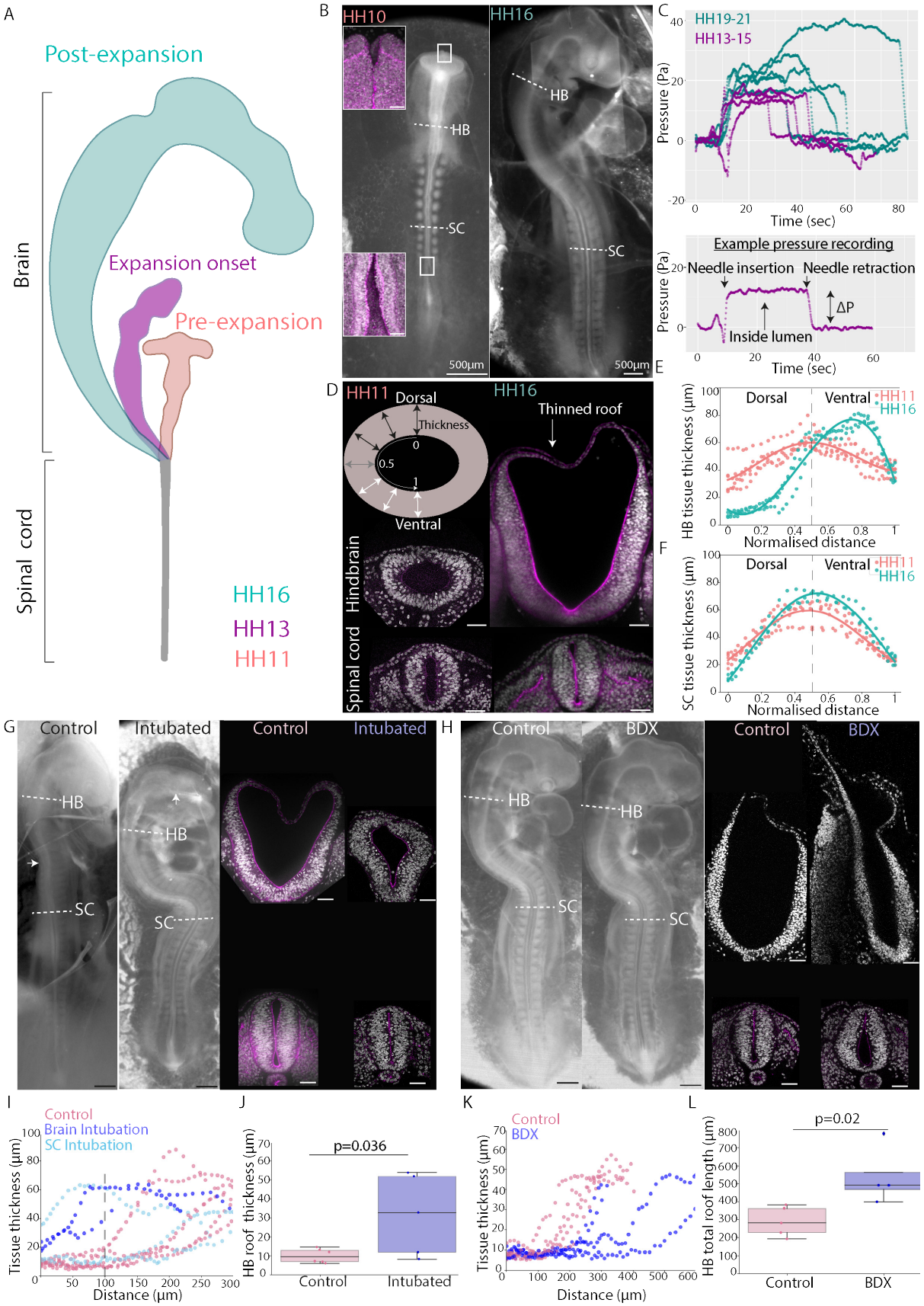

413

Figure 1. Neural tube lumen pressure drives hindbrain and spinal cord shape divergence

(A) Schematic depicting brain expansion during chicken embryo development, Hamburger and Hamilton stages of development are given. (B-F) Lumen pressure increase and dorsal tissue thinning occur concomitantly with brain expansion. (B) Bright-field images of chicken embryos prior to brain expansion (HH10) and following brain expansion (HH16) and confocal microscopy images of the early anterior and posterior neuropore at the level of the white boxes. (C) Pressure readings obtained by inserting a microneedle connected to a pressure sensor into the neural tube lumen in embryos at the onset of and following brain expansion. (D) Schematic showing tissue thickness measurement approach and confocal microscopy images of neural tube cross-sections taken at the level of the dashed white lines in (B). (E) Apical-basal tissue thickness along the hindbrain lumen circumference, n=6 hh11 embryos, n=3 HH16 embryos. (F) Apical-basal tissue thickness along the spinal cord lumen circumference, n=6 hh11 embryos, n=3 HH16 embryos. (G-L) Pressure decrease and increase experiments. (G) Bright-field images of control and intubated embryos at ~20 hours post-intubation and confocal images of corresponding hindbrain and spinal cord cross-sections. (H) Bright-field images of control and β-D-xyloside (BDX) treated embryos ~20h post treatment and corresponding confocal images of hindbrain and spinal cord cross-sections. (I) Tissue thickness along the hindbrain circumference moving from dorsal to ventral in control, anterior intubated and spinal cord intubated embryos. (J) Hindbrain roof thickness (averaged over the first 100µm from the dorsal midpoint in control (n=6), anterior intubated (n=2) and spinal cord intubated (n=3) embryos. (K) Tissue thickness along the hindbrain circumference in control and BDX treated embryos. (L) Hindbrain total roof length in control (n=5) and BDX treated (n=4) embryos.

Black scale bars are 500µm, white scale bars are 50µm unless otherwise stated.

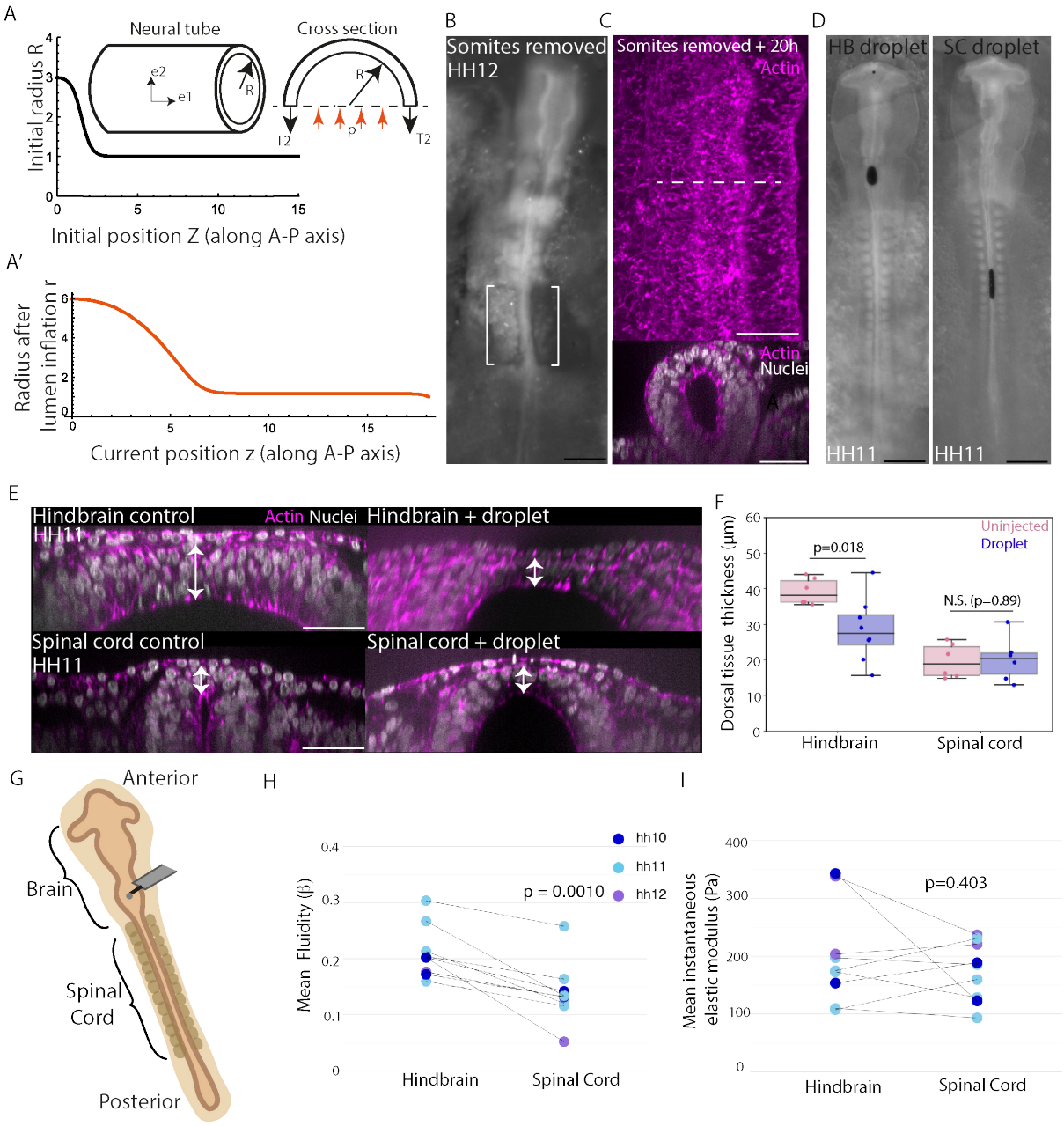

Figure 2. The dorsal hindbrain is more deformable than the dorsal spinal cord prior to brain expansion

(A-A') A physical model predicts a greater degree of expansion in regions with initially larger radius. A cellularised model of an epithelial tube was used to determine how the initial radius at a point along the tube may affect its expansion dynamics under internal pressure. The anterior neural tube is positioned at z = 0. (B-C) Lateral tissue removal experiments. (B) Bright-field image of a pre-brain expansion stage embryo with posterior somites and anterior presomitic mesoderm removed (n=4, control n=3). (C) Confocal images of the dorsal surface view and cross-section view of the spinal cord

in a ~20h post somite-removal embryo. (D-F) Dorsal tissue deformation under ferrofluid droplet injection. (D) Widefield images of HH11 stage embryos with ferrofluid droplet injections in either the hindbrain or spinal cord lumen. (E) Confocal images showing cross-sectional views of the spinal cord and hindbrain in HH10-11 stage uninjected embryos (n=6 spinal cord, n=6 hindbrain) and embryos with ferrofluid droplets injected into either the hindbrain or spinal cord (n=6 hindbrain, n=8 spinal cord). White arrows indicate thickness measurements (acquired at the thinnest dorsal point observable). (F) Quantification of hindbrain and spinal cord roof thickness in uninjected and droplet injected embryos. (G-I) Atomic force microscopy experiments. (G) Schematic depicting atomic force microscopy measurement set up. (H) Mean Beta value (corresponding to fluidity) of the hindbrain and spinal cord in HH10, 11 and 12 embryos (n=9). (I) Mean instantaneous elastic modulus of the hindbrain and spinal cord in HH10, 11 and 12 embryos (n=9).

Black scale bars are 500µm. White scale bars are 50µm.

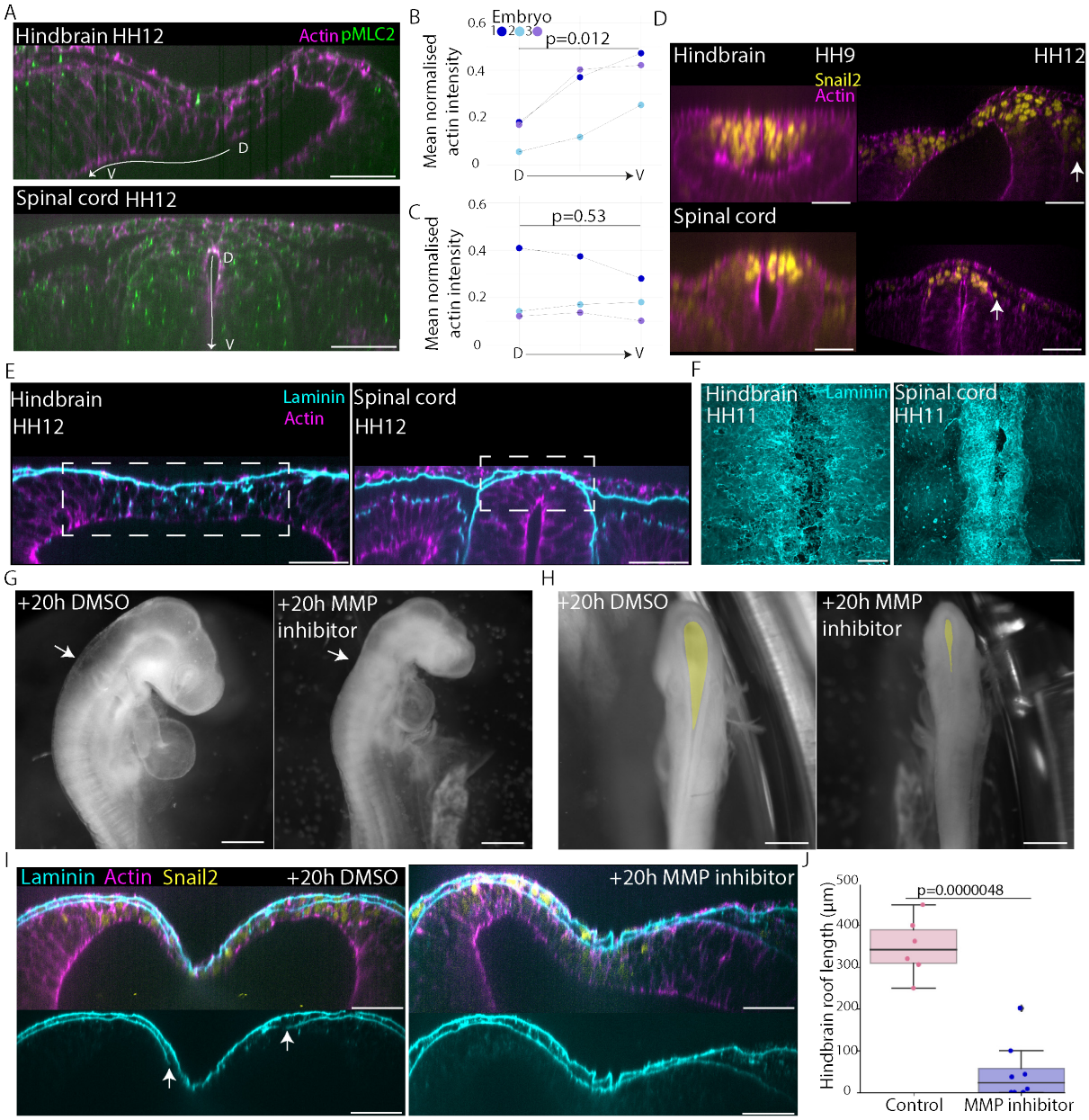

Figure 3. Differential neural crest cell behaviour underlies the acquisition of a thinned out and expanded dorsal hindbrain roof

(A-C) Actomyosin localisation in the dorsal hindbrain and spinal cord. (A) Confocal images of actin and phosphorylated myosin light chain kinase II in the hindbrain and spinal cord of HH12 stage embryos. (B) Quantification of apical actin signal intensity along the lumen circumference in the hindbrain of HH11 and HH12 stage embryos. (C) Quantification of apical actin signal intensity along the lumen circumference in the spinal cord of HH11 and HH12 stage embryos. (D) Premigratory neural crest in the hindbrain and spinal cord. Confocal images showing Snail2+ cell migration in the

466 hindbrain and spinal cord cross sections of embryos progressing towards brain-expansion stages
467 (HH9 to HH12). (E-F) ECM organisation in the dorsal hindbrain and spinal cord. (E) Confocal images
468 showing laminin and actin organisation in cross sections of the spinal cord and hindbrain of HH12
469 stage embryos. F) Confocal images showing laminin organisation at the dorsal surface in a 3D
470 rendering of the spinal cord and hindbrain of HH11 stage embryos. (G-H) ECM remodelling
471 perturbation experiments. (G) Brightfield images of embryos treated with DMSO or MMP inhibitor at
472 HH11 and incubated for 20 hours. White arrows indicate hindbrain at level of otic vesicle. (H) Dorsal
473 views of DMSO and MMP inhibitor treated embryos. Yellow highlight fills the brain dorsal surface. (I)
474 Confocal images showing the dorsal hindbrain of control (n=3) and MMP inhibitor treated embryos
475 (n=5), ~20 hours post treatment. Bottom panels show laminin surface with white arrows indicating
476 breaks in laminin continuity. (J) Hindbrain roof length obtained by measuring the length of the single-
477 cell thick roof in control and inhibitor treated embryos. White scale bars are 50µm.

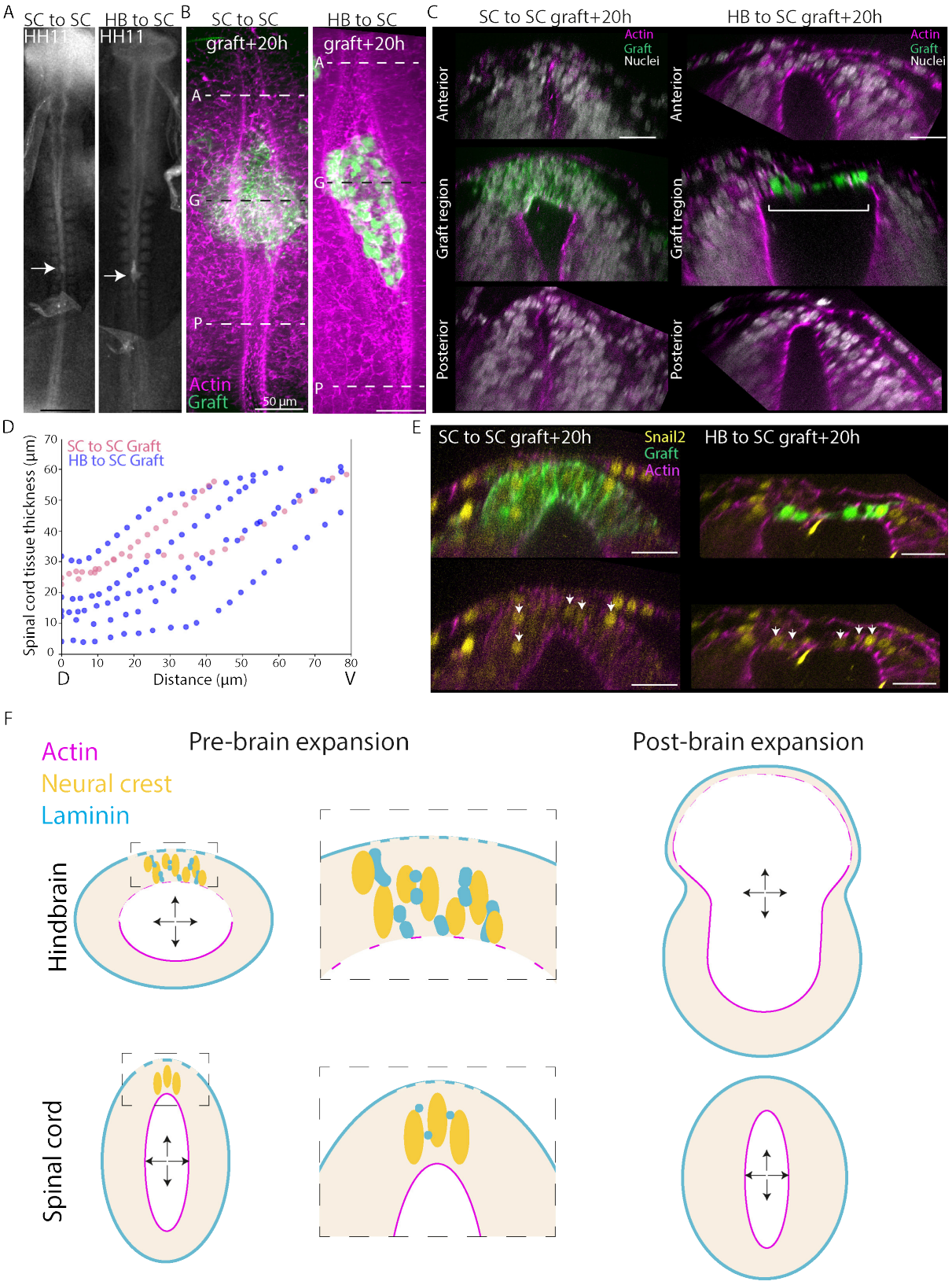

Figure 4. Premigratory neural crest cells in the dorsal hindbrain are sufficient to generate a thinned dorsal roof and neural tube expansion

(A-E) Grafting experiments. (A) Bright-field image of pre-brain expansion stage (HH11) embryos with a spinal cord-to-spinal cord graft (n=2) or a hindbrain-to-spinal cord graft (n=5). (B) Confocal images showing dorsal surface view of spinal cord-to-spinal cord and hindbrain-to-spinal cord graft integration ~20 hours post-grafting. (C) Confocal images showing cross-sectional views of spinal cord-to-spinal cord and hindbrain-to-spinal cord graft integration ~20 hours post-grafting. Cross section levels correspond to dashed lines in (B). White bracket highlights the thinned-out roof in the graft region. D) Spinal cord tissue thickness in the region with spinal cord or hindbrain grafted cells (thickness measurements taken along lumen circumference going from dorsal midpoint and moving ventrally). (E) Confocal images showing Snail2+ cells in graft regions. White arrows indicate Snail2+ cells within the GFP+ graft. (F) Schematic depicting proposed model of brain expansion relative to the spinal cord. Premigratory neural crest cells in pre-brain expansion stage embryos show differences in their behaviour between the hindbrain and spinal cord regions of the neural tube. A greater extent of mesenchymal behaviour and corresponding extracellular matrix remodelling underlies a more deformable dorsal roof in the hindbrain compared to the spinal cord. This allows the hindbrain roof to deform more under internal lumen pressure, driving hindbrain expansion relative to the spinal cord during early embryo development.

Black scale bars are 500µm. White scale bars are 25µm unless otherwise stated.

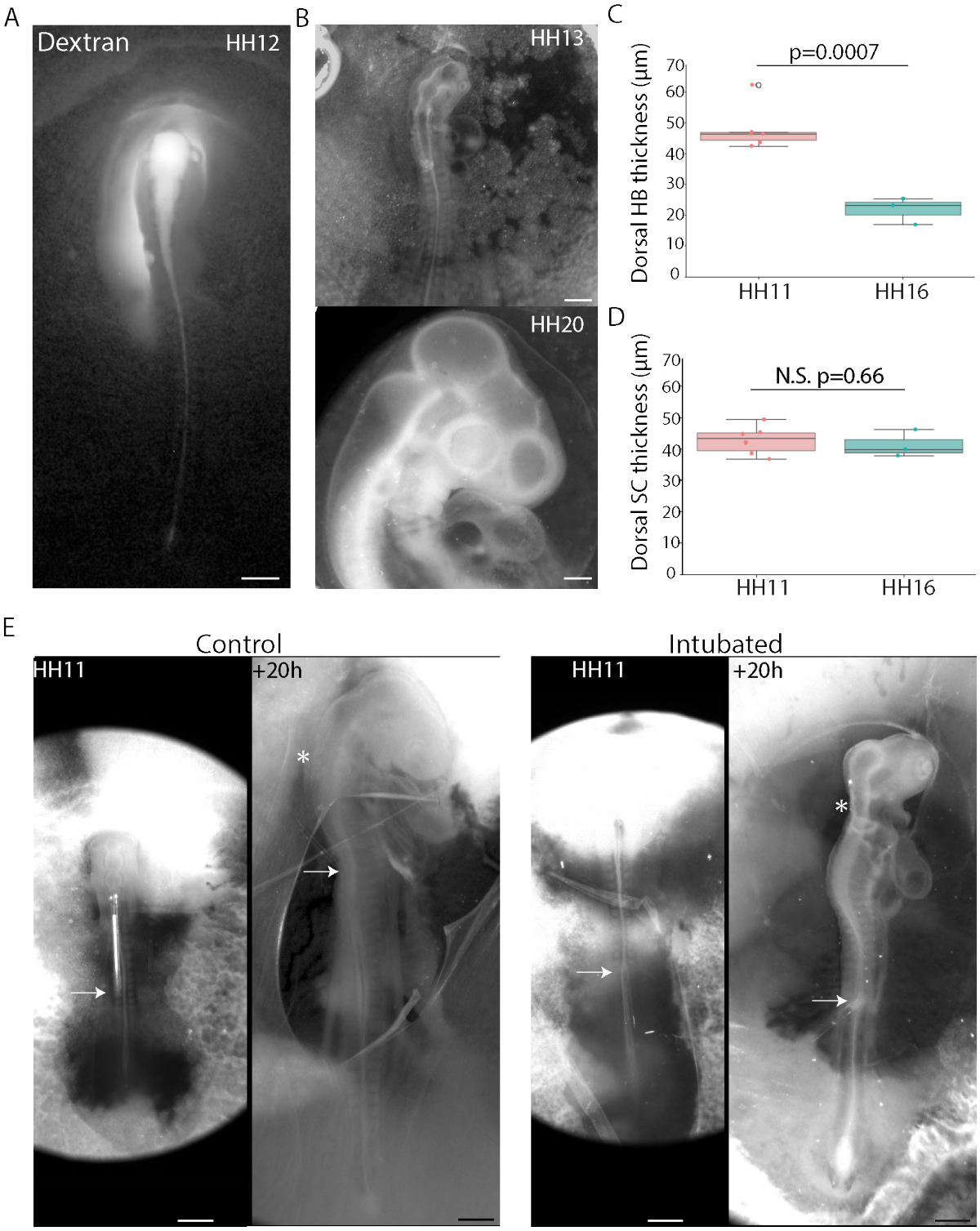

Figure S1. Neural tube characterisation and intubation experiments

(A) An HH12 stage embryo injected in the neural tube lumen with fluorescent Dextran. (B) Brightfield images of the anterior of embryos used in pressure measurements. (C) Mean thickness of the dorsal hindbrain in HH11 and HH16 stage embryos. (D) Mean thickness of the dorsal hindbrain in HH11 and

503 HH16 stage embryos. (E) Brightfield images of control and intubated embryos just after intubation

504 and 20 hours later. White arrows mark site of intubation. White asterisks mark the hindbrain.

505 All scale bars are 500µm.

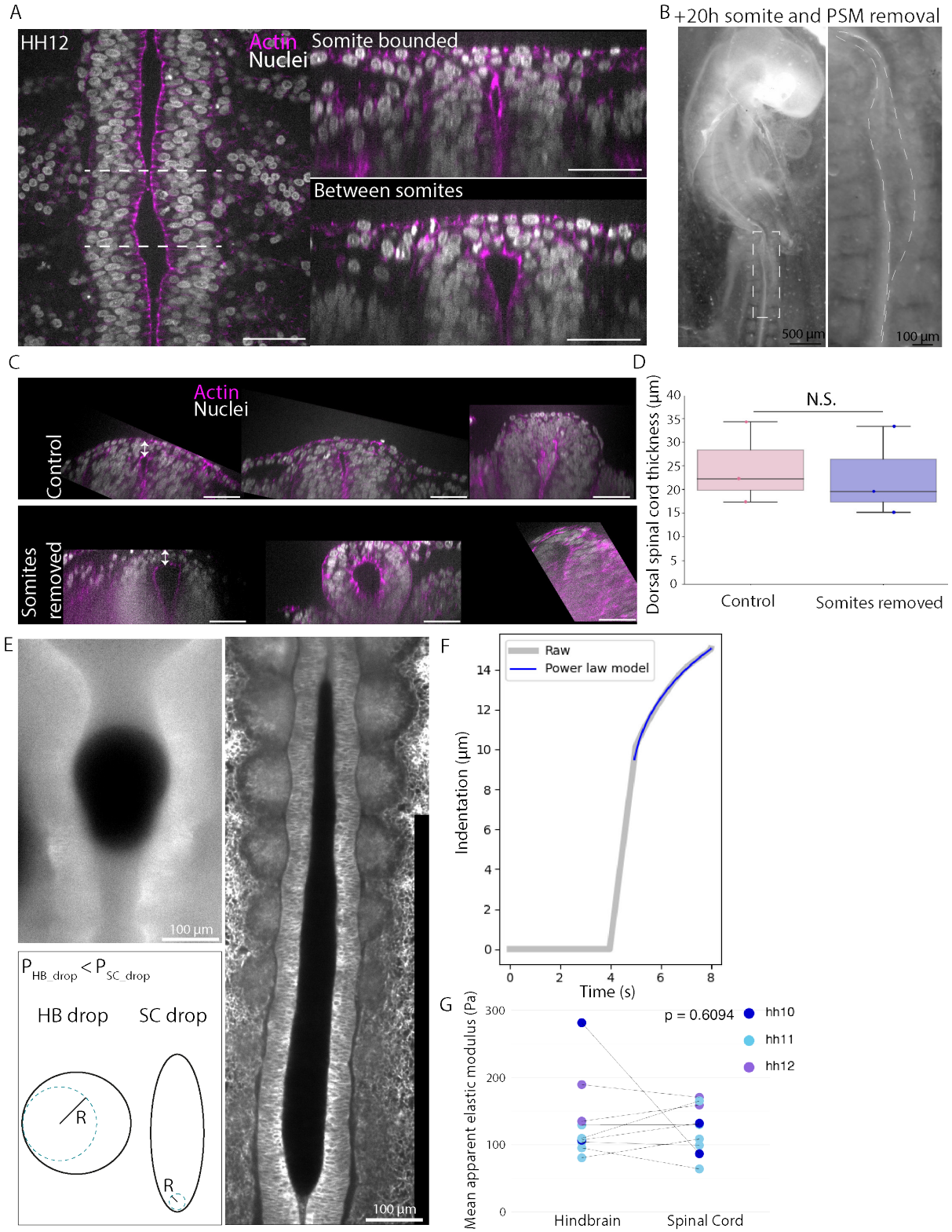

506

507 **Figure S2. Geometry and tissue mechanics experiments**

(A) Confocal images of dorsal and cross-sectional views of the spinal cord region in an HH12 stage embryo. Dashed lines indicate level of cross-sectional views. (B) A widefield image of an embryo ~20 hours after posterior somite and PSM removal with zoomed-in view of the widened spinal cord region. (C) Confocal images of cross-sectional views of the spinal cord in embryos 20 hours after control cuts or somite removal. (D) Dorsal spinal cord thickness in control and somite removed embryos, measured at the dorsal midpoint. (E) Close up views of ferrofluid droplets in the hindbrain and spinal cord and a schematic illustrating the higher curvature at the droplet-lumen interface and thus higher pressure exerted by droplets in the spinal cord region compared to the hindbrain region. (F) Fitting of AFM indentation data to extract fluidity ‘β’. G) Mean elastic modulus in the hindbrain and spinal cord of HH10, 11 and 12 stage embryos.

White scale bars are 50µm unless otherwise stated.

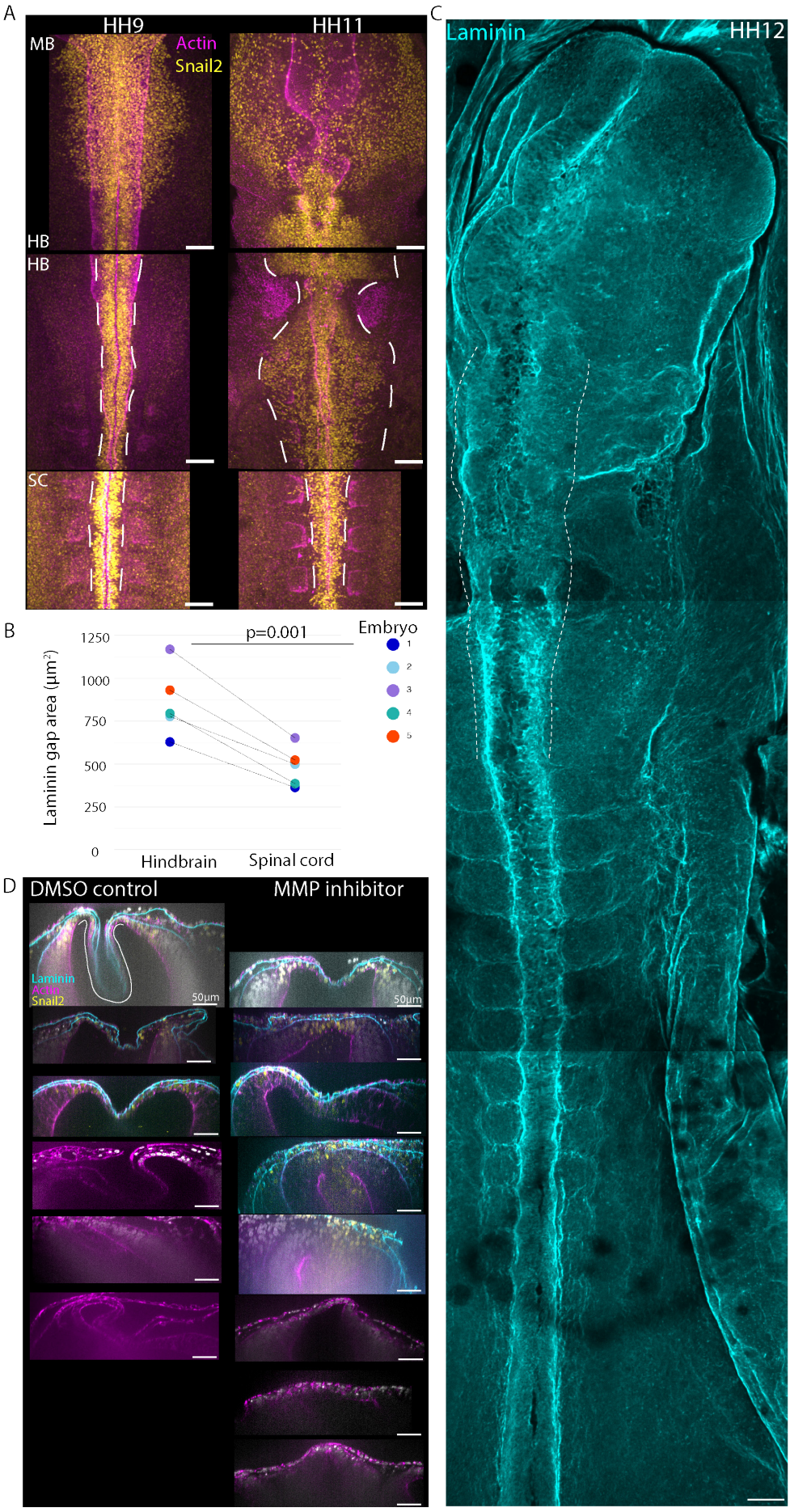
A
HH9
HH11
MB
Actin
Snail2
HB
HB
SC
B
p=0.001
Embryo
1
2
3
4
5
Laminin gap area (µm²)
1250
1000
750
500
250
0
Hindbrain
Spinal cord
C
Laminin
HH12
D
DMSO control
MMP inhibitor
Laminin
Actin
Snail2
50µm
50µm

Figure S3. Neural crest and ECM experiments

(A) Confocal images showing Snail2+ cells at the dorsal surface of HH9 and HH11 stage brain and spinal cord regions. Dashed lines depict the extent of Snail2+ cell spreading away from the dorsal midline. (B) Total area of gaps in ECM on the dorsal surface of the hindbrain and spinal cord of pre-brain expansion embryos. (C) Confocal images stitched together to show a 3D rendering of the laminin matrix in a HH12 stage embryo. Dashed lines depict the boundaries of the hindbrain region. (D) Confocal images of DMSO and MMP inhibitor treated embryo hindbrains, ~20 hours post treatment.

White scale bars are 100µm unless otherwise stated.

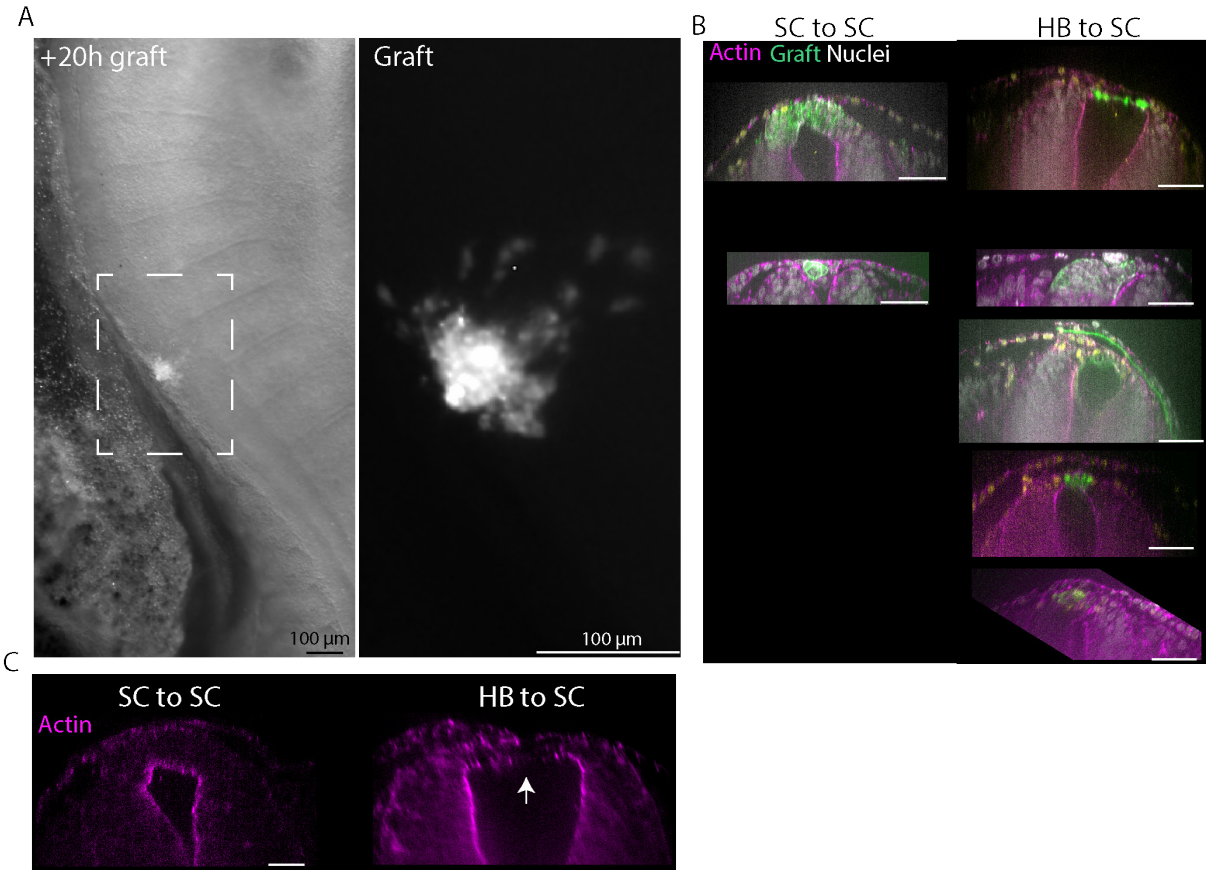

Figure S4. Graft experiments

(A) Widefield images of an embryo ~20 hours after introduction of a GFP+ graft into the spinal cord and a zoomed-in view of the graft region. (B) Confocal images of cross-sectional views of the spinal cord at spinal cord-spinal cord and hindbrain-spinal cord graft sites. (C) Confocal images showing

actin organisation at the apical lumen surface in a spinal cord-spinal cord graft region and a hindbrain-spinal cord graft region. White arrow indicates loss of apical actin localisation. White scale bars are all 50µm unless otherwise stated.

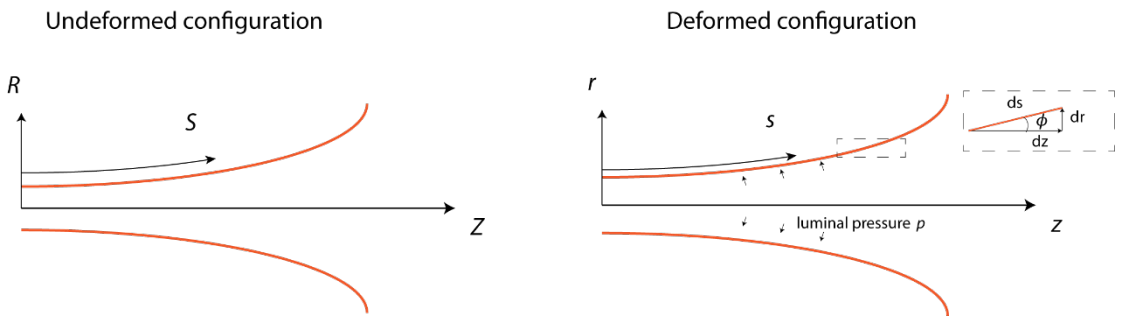

Figure S5. Theoretical model of neural tube expansion under pressure

A schematic showing the initial undeformed configuration (left) and the current deformed configuration (right) pressurized with luminal fluids.

References:

1. Sugahara, F. *et al.* Evidence from cyclostomes for complex regionalization of the ancestral vertebrate brain. *Nature* **531**, 97–100 (2016).
2. Kotrschal, A. *et al.* Artificial Selection on Relative Brain Size in the Guppy Reveals Costs and Benefits of Evolving a Larger Brain. *Curr Biol* **23**, 168–171 (2013).
3. Sol, D., Duncan, R. P., Blackburn, T. M., Cassey, P. & Lefebvre, L. Big brains, enhanced cognition, and response of birds to novel environments. *Proceedings of the National Academy of Sciences* **102**, 5460–5465 (2005).
4. del Corral, R. D. *et al.* Opposing FGF and Retinoid Pathways Control Ventral Neural Pattern, Neuronal Differentiation, and Segmentation during Body Axis Extension. *Neuron* **40**, 65–79 (2003).
5. Nordström, U., Jessell, T. M. & Edlund, T. Progressive induction of caudal neural character by graded Wnt signaling. *Nat Neurosci* **5**, 525–532 (2002).

555 6. Bel-Vialar, S., Itasaki, N. & Krumlauf, R. Initiating Hox gene expression: in the early chick
556 neural tube differential sensitivity to FGF and RA signaling subdivides the HoxBgenes in
557 two distinct groups. *Development* **129**, 5103–5115 (2002).
558 7. Colas, J.-F. & Schoenwolf, G. C. Towards a cellular and molecular understanding of
559 neurulation. *Developmental Dynamics* **221**, 117–145 (2001).
560 8. Hamburger, V. & Hamilton, H. L. A series of normal stages in the development of the
561 chick embryo. *Developmental Dynamics* **195**, 231–272 (1992).
562 9. Tallinen, T. *et al.* On the growth and form of cortical convolutions. *Nature Physics* **12**,
563 588–593 (2016).
564 10. Mota, B. & Herculano-Houzel, S. Cortical folding scales universally with surface area and
565 thickness, not number of neurons. *Science* **349**, 74–77 (2015).
566 11. Desmond, M. E. & Jacobson, A. G. Embryonic brain enlargement requires cerebrospinal
567 fluid pressure. *Developmental Biology* **57**, 188–198 (1977).
568 12. Garcia, K. E., Stewart, W. G., Espinosa, M. G., Gleghorn, J. P. & Taber, L. A. Molecular and
569 mechanical signals determine morphogenesis of the cerebral hemispheres in the chicken
570 embryo. *Development* **146**, dev174318 (2019).
571 13. Le Douarin, N. M. Cell Line Segregation During Peripheral Nervous System Ontogeny.
572 Science **231**, 1515-1522 (1986)
573 14. Garcia, K. E., Okamoto, R. J., Bayly, P. V. & Taber, L. A. Contraction and stress-dependent
574 growth shape the forebrain of the early chicken embryo. *Journal of the Mechanical*
575 *Behavior of Biomedical Materials* **65**, 383–397 (2017).
576 15. Schoenwolf, G. C. Observations on closure of the neuropores in the chick embryo.
577 *American Journal of Anatomy* **155**, 445–465 (1979).

578 16. Desmond, M. E., Levitan, M. L. & Haas, A. R. Internal luminal pressure during early chick
579 embryonic brain growth: Descriptive and empirical observations. *The Anatomical Record*
580 *Part A: Discoveries in Molecular, Cellular, and Evolutionary Biology* **285A**, 737–747
581 (2005).
582 17. Alonso, M. I., Gato, A., Moro, J. A. & Barbosa, E. Disruption of proteoglycans in neural
583 tube fluid by β-D-xyloside alters brain enlargement in chick embryos. *Anat. Rec.* **252**,
584 499–508 (1998).
585 18. Xiong, F., Ma, W., Bénazéraf, B., Mahadevan, L. & Pourquié, O. Mechanical Coupling
586 Coordinates the Co-elongation of Axial and Paraxial Tissues in Avian Embryos.
587 *Developmental Cell* **55**, 354-366.e5 (2020)
588 19. Shellard, A., Szabó, A., Trepat, X. & Mayor, R. Supracellular contraction at the rear of
589 neural crest cell groups drives collective chemotaxis. *Science* **362**, 339–343 (2018).
590 20. Berndt, J. D., Clay, M. R., Langenberg, T. & Halloran, M. C. Rho-kinase and myosin II affect
591 dynamic neural crest cell behaviors during epithelial to mesenchymal transition in vivo.
592 *Developmental Biology* **324**, 236–244 (2008).
593 21. Scarpa, E. *et al.* Cadherin Switch during EMT in Neural Crest Cells Leads to Contact
594 Inhibition of Locomotion via Repolarization of Forces. *Developmental Cell* **34**, 421–434
595 (2015).
596 22. Theveneau, E., Duband, J.-L. & Altabef, M. Ets-1 Confers Cranial Features on Neural Crest
597 Delamination. *PLoS ONE* **2**, e1142. (2007)
598 23. Rocha, M. *et al.* From head to tail: regionalization of the neural crest. *Development* **147**,
599 dev193888 (2020).

600 24. Taneyhill, L. A., Coles, E. G. & Bronner-Fraser, M. Snail2 directly represses cadherin6B
601 during epithelial-to-mesenchymal transitions of the neural crest. *Development* **134**,
602 1481–1490 (2007).
603 25. Nieto, M. A., Sargent, M. G., Wilkinson, D. G. & Cooke, J. Control of Cell Behavior During
604 Vertebrate Development by Slug, a Zinc Finger Gene. *Science* **264**, 835–839 (1994).
605 26. Cai, D. H., Vollberg Sr., T. M., Hahn-Dantona, E., Quigley, J. P. & Brauer, P. R. MMP-2
606 expression during early avian cardiac and neural crest morphogenesis. *The Anatomical*
607 *Record* **259**, 168–179 (2000).
608 27. Monsonego-Ornan, E. *et al.* Matrix metalloproteinase 9/gelatinase B is required for
609 neural crest cell migration. *Developmental Biology* **364**, 162–177 (2012).
610 28. Elosegui-Artola, A. *et al.* Matrix viscoelasticity controls spatiotemporal tissue
611 organization. *Nat. Mater.* **22**, 117–127 (2023).
612 29. Crest, J., Diz-Muñoz, A., Chen, D.-Y., Fletcher, D. A. & Bilder, D. Organ sculpting by
613 patterned extracellular matrix stiffness. *Elife* **6**, e24958 (2017).
614 30. Gans, C. & Northcutt, R. G. Neural Crest and the Origin of Vertebrates: A New Head.
615 *Science* **220**, 268–273 (1983).
616 31. Couly, G., Grapin-Botton, A., Coltey, P. & Le Douarin, N. M. The regeneration of the
617 cephalic neural crest, a problem revisited: the regenerating cells originate from the
618 contralateral or from the anterior and posterior neural fold. *Development* **122**, 3393–
619 3407 (1996).
620 32. Campo-Paysaa, F., Clarke, J. D. & Wingate, R. J. Generation of the squamous epithelial
621 roof of the 4th ventricle. *Elife* **8**, e38485 (2019)
622 33. Mosaliganti, K. R. *et al.* Size control of the inner ear via hydraulic feedback. *Elife* **8**, 2837
623 (2019).

34. Chan, C. J. *et al.* Hydraulic control of mammalian embryo size and cell fate. *Nature* **571**, 112–116 (2019).
35. Dumortier, J. G. *et al.* Hydraulic fracturing and active coarsening position the lumen of the mouse blastocyst. *Science* **365**, 465–468 (2019).
36. Nelson, C. M., Gleghorn, J. P., Pang, M. F., & 2017. Microfluidic chest cavities reveal that transmural pressure controls the rate of lung development. *Development* **144**, 4328-4335 (2017)
37. McGrew, M. J. *et al.* Localised axial progenitor cell populations in the avian tail bud are not committed to a posterior Hox identity. *Development* **135**, 2289–2299 (2008).
38. Rozbicki, E. *et al.* Myosin-II-mediated cell shape changes and cell intercalation contribute to primitive streak formation. *Nat Cell Biol* **17**, 397–408 (2015).
39. Chapman, S. C., Collignon, J., Schoenwolf, G. C. & Lumsden, A. Improved method for chick whole-embryo culture using a filter paper carrier. *Dev Dyn* **220**, 284–289 (2001).
40. Kunz, D. *et al.* Downregulation of extraembryonic tension controls body axis formation in avian embryos. *Nat Commun* **14**, 3266 (2023).
41. McLaren, S. B. P. & Xiong, F. Lumen pressure modulation in chicken embryos. bioRxiv 569177 (2023).
42. Thompson, A. J. *et al.* Rapid changes in tissue mechanics regulate cell behaviour in the developing embryonic brain. *Elife* **8**, e39356 (2019).
43. Schierbaum, N., Rheinlaender, J. & Schäffer, T. E. Combined atomic force microscopy (AFM) and traction force microscopy (TFM) reveals a correlation between viscoelastic material properties and contractile prestress of living cells. *Soft Matter* **15**, 1721–1729 (2019).

44. Schindelin, J. *et al.* Fiji: an open-source platform for biological-image analysis. *Nat Methods* **9**, 676–682 (2012).

45. Ahlers, J. *et al.* napari: a multi-dimensional image viewer for Python. (2023)

46. Kyriakides, S. & Yu-Chung, C. The initiation and propagation of a localized instability in an inflated elastic tube. *International Journal of Solids and Structures* **27**, 1085–1111 (1991).